ACS Partner Journal

CHEMICAL & BIOMEDICAL IMAGING

pubs.acs.org/ChemBioImaging

Article

High-Throughput, Low Background, and Wide-Field Microscopy by Flat-Field Photobleaching Imprinting Microscopy

Yizhi Qin, Mengling Zhang, Huiwen Hao, Boxin Xue, Jiahao Niu, and Yujie Sun*

Cite This: *Chem. Biomed. Imaging* 2023, 1, 843−851

Read Online

ACCESS | Metrics & More | Article Recommendations | Supporting Information

ABSTRACT: Wide-field photobleaching imprinting microscopy (PIM) can improve fluorescence image contrast by cleverly exploiting the fluorophores' photobleaching properties. However, as conventional wide-field PIM commonly adopts Gaussian illumination with a nonuniform lateral fluence distribution, the field-of-view (FOV) and sampling density are largely reduced. In addition, the slow axial fluence gradient of Gaussian illumination limits the signal-to-background ratio (SBR) improvement and optical sectioning capability of PIM. Here, we present flat-field photobleaching imprinting microscopy (ffPIM) with a uniform lateral excitation fluence and sharp axial intensity gradient at the focal plane. ffPIM demonstrates low background, large FOV, and thin optical section. More importantly, compared to either conventional wide-field PIM or light-sheet microscopy, ffPIM shows much better balance for FOV, sampling density, SBR, and optical sectioning capability. The performance of ffPIM is characterized by simulation and resolving multiple cellular structures. Finally, ffPIM can be easily implemented to a standard commercial wide-field microscope and, thereby, allow general laboratories to benefit from this technique.

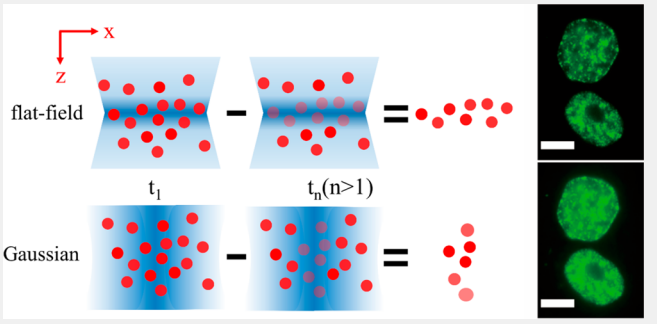

KEYWORDS: *Photobleaching imprinting microscopy, Wide-field microscopy, Flat-field illumination, Background-free fluorescence imaging, High-throughput, Optical section*

INTRODUCTION

Fluorescence microscopy is an important tool for biological research.[1] Moreover, 3D imaging capabilities are indispensable in the study of developmental and cell biology, anatomy, biophysics, and neuroscience. 3D imaging is commonly realized through three different strategies. The first is based on illumination (e.g., light-sheet microscopy,[2] confocal microscopy,[3] and two-photon and multiphoton microscopy[4]). In confocal microscopy, a pinhole conjugated to the objective's focal plane is used to suppress the out-of-focus signal, which is the main contribution of the background. Removing the out-of-focus signal can improve the signal-to-background ratio. However, the illumination still excites all fluorescence within the depth of field (DOF) of the acquisition objective, and the pinhole not only suppresses the out-of-focus signal but also affects the acquisition of the signal at the focal plane, which limits the improvement of the signal-to-background ratio. Light-sheet fluorescence microscopy (LSFM), also named selective-plane illumination microscopy, uses a pair of orthogonally placed objectives with one objective for illumination and the other one for detection. The light sheet illuminates a layer of the sample, and an objective orthogonal to it collects the fluorescence. Because only the fluorescence near the focal plane of the detection objective is excited, light-sheet microscopy has an intrinsic advantage in suppressing the out-of-focus background. However, almost all light-sheet microscopes require at least two objectives, and the steric hindrance between the two objectives results in sacrifice either in the resolving performance (low NA, long working distance objective) or in the operation feasibility of the system. In recent years, several groups have developed single objective light-sheet systems[5−7] that allow the LSFM to operate like an inverted fluorescence microscope and accept traditional biological samples. Such systems typically utilize an oblique illumination pattern. This oblique plane is corrected by a pair of objectives[6,8−13] in the detection path so that all light reaches the focal point of the camera. However, the correction module results in a loss of the numerical aperture, and a high numerical aperture is essential to achieve resolution in subcellular imaging. The second strategy for 3D fluorescence microscopic imaging is based on detection, such as light field fluorescence microscopy[14] and point spread function (PSF) engineering.[15−17] These techniques make full use of the acquired

Received: July 6, 2023
Revised: October 8, 2023
Accepted: October 9, 2023
Published: October 28, 2023

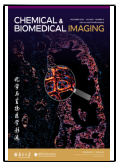

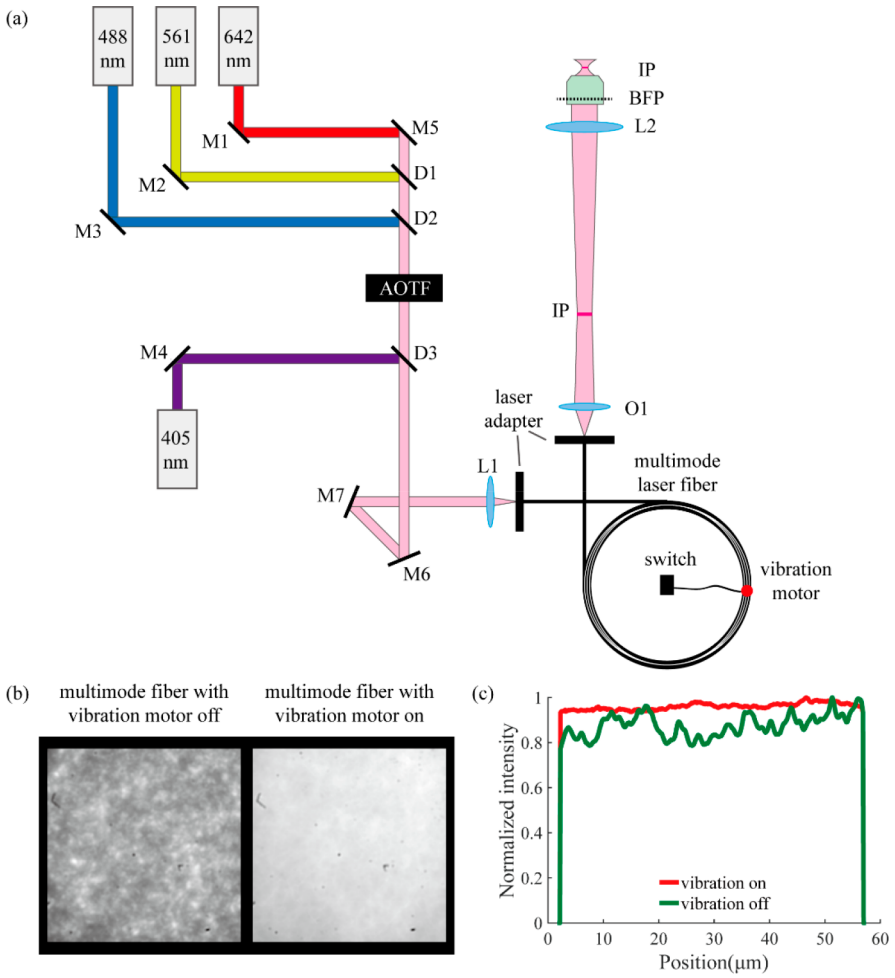

Figure 1. Schematic and characterization of flat-field microscopy. (a) Schematic of flat-field microscopy. A uniform square spot is formed by a customized multimode fiber bound with a vibration motor. The square spot is focused at the focal plane of the objective. M1−M6: aluminum mirrors (Thorlabs); D1−D3: dichroic mirrors; O1: objective (10×/NA0.25, Olympus); L1: lens (AC050-010-A-ML, Thorlabs); L2: lens (AC254-250-A-ML, Thorlabs). The objective used for detection is an objective lens (Plan Apo 100×, 1.49 oil immersion, Nikon). The fiber (WFANS 200 × 200/238 × 238, CeramOptec) is specially designed for large-field illumination. The elements not shown in the figure are Eclipse Ti-E microscope (Nikon) and DU-897D EMCCD (Andor). (b, c) The illumination pattern of the multimode fiber has speckles. Vibrating the fiber can eliminate speckles, generating a more uniform illumination.

fluorescence signal and achieve 3D imaging by matching the signal to its actual depth. However, these methods require complex optical design, and few commercial microscopes are available, limiting their use in biological research laboratories. The third strategy is based on computation. For example, deconvolution microscopy (DM) restores the actual image of the object that is distorted by the imaging system in the imaging process due to imperfection and finite aperture of any lenses.[18] A successful deconvolution process depends on the accuracy of the image data and the estimated PSF. The most critical step of the deconvolution method is not the computation, but the acquisition of accurate, artifact-free, and high signal-to-noise images.[19] This limits DM to specimens with a signal-to-background ratio (SBR) not less than 1:20.[20] In addition, mismatched PSFs or low signal-to-noise ratio images may produce artifacts and reduce image recovery quality.[21]

Photobleaching imprinting microscopy (PIM) is a computational imaging method based on the principle that the photobleaching rate of a fluorophore is proportional to the local illumination power density. It utilizes two sets of a priori information to achieve optical sectioning and improve the SBR.[22−27] One is the photobleaching property of the fluorophore itself, and the second is the illumination pattern of the imaging system. Different from DM, where the PSF of the system needs to be calibrated in advance, PIM is based on fitting higher-order components from a series of time-lapse images. Hence, in principle, PIM has fewer artifacts than DM. However, as a good PIM image relies on a proper light fluence distribution at the focal plane, conventional wide-field microscopy with Gaussian illumination is not ideal for PIM. First, the light fluence distribution of Gaussian illumination is nonuniform in the $x-y$ plane, causing the effective field-of-view (FOV) to be limited within the central region where the PIM computation is also approximated to constant light fluence. Second, for fluorophores that are in the peripheral region of the Gaussian illumination, the photobleached portions are wasted as they are not used for PIM computation, sacrificing the overall sampling density of the image. Third, the light intensity gradient at the focal plane is less sharp than that out of the focal plane, which limits the signal-to-background ratio improvement of PIM with Gaussian illumination. In this work, we developed flat-field photobleaching imprinting microscopy (ffPIM), a PIM method based on uniform illumination that

https://doi.org/10.1021/cbmi.3c00079
Chem. Biomed. Imaging 2023, 1, 843−851

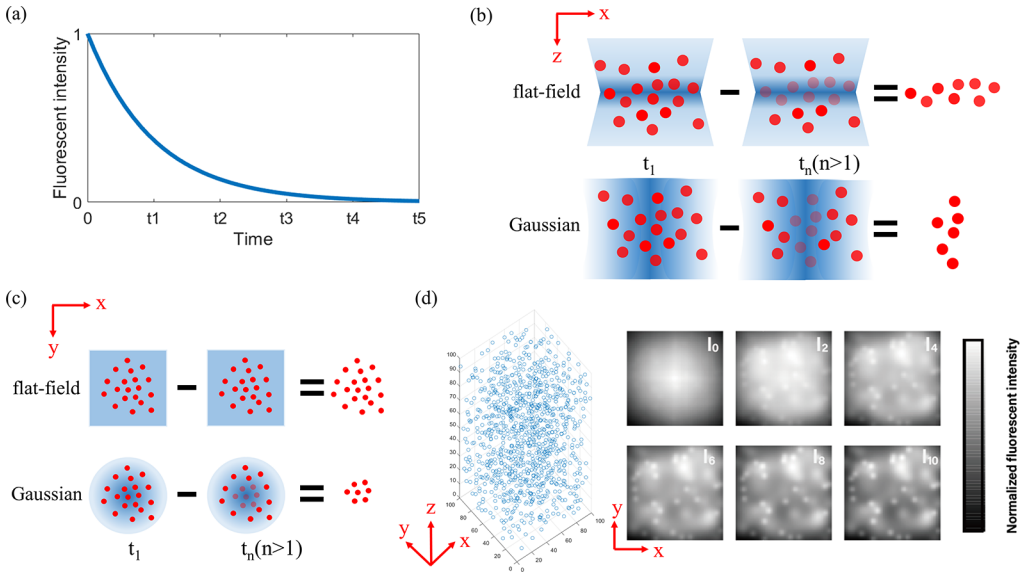

Figure 2. Operation principle of flat-field PIM (ffPIM). (a) Photobleaching rate obeys a single-exponential temporal decay law. (b, c) Comparison between ffPIM and conventional wide-field PIM. (d) Simulation results of ffPIM. I_0 represents a wide-field image of a 3D sample consisting of 100 randomly distributed fluorescent beads in 100 × 100 × 100 volume. I_2 to I_{10} are different high-order ffPIM images.

overcomes the limitations caused by Gaussian illumination. The excitation fluence of ffPIM is uniform in the $x-y$ plane and has a maximum intensity in the focal plane. We compared ffPIM with conventional wide-field PIM with Gaussian illumination. It shows that ffPIM has a better optical section capability. ffPIM can maintain a large FOV equal to the FOV of the original images. Moreover, it avoids wasting fluorophores and improves the sampling density. We also compared ffPIM with light-sheet microscopy. It shows that ffPIM has a better optical sectioning performance than light-sheet microscopy with a high-NA objective. In addition, ffPIM has a large FOV that light sheets with the same optical sectioning cannot achieve, greatly compensating for the drawback of the light sheet.

RESULTS AND DISCUSSION

Flat-Field Illumination

Uniform illumination is very important in wide-field microscopy, especially in quantitative analysis.[28] There are three main strategies to achieve uniform illumination. One is based on a beamshaper.[28−31] However, this device is expensive, and its wavelength dependence makes the method unsuitable for multicolor imaging. The second strategy is based on the method of Kohler illumination, using a diffuser and a pair of microlens arrays to achieve a uniform distribution of light in the focal plane of the objective.[32,33] This method requires a complex optical design and is thus difficult to adopt in common laboratories. The third method is based on multimode fiber combined with a diffuser[34] or vibrating elements[35] in the optical path.

In our system, we used a customized homogenizing multimode fiber with a square core to generate uniform illumination. The optical setup of flat-field microscopy is shown in Figure 1. Light from the optical coupling system passed through an objective O1 to form a square spot. The square spot was reduced and focused on the sample plane by lens L2 and an objective. The size of the FOV can be adjusted by changing the focal length of L2. For example, a shorter focal length can create a larger FOV.

Unlike common wide-field microscopes, which focus the light at the back focal plane of the objective, our system collimated light through the back focal plane of the objective and eventually focused a square spot at the focal plane of the objective. As a result, we obtained an excitation fluence with a uniform intensity distribution in the $x-y$ plane and a maximum intensity in the z direction at the focal plane of the objective, which is ideal for a large FOV and good optical sectioning capability.

Theory and Simulation

As described previously,[22] PIM works simply by time-lapse imaging of photobleaching-induced fluorescent decay that is dependent on the local excitation fluence. For wide-field PIM with one-photon excitation, the local fluorescence intensity is the integration of all fluorescence along the axial direction.

$$I(x, y) = C \int \mu_a(x, y, z) F(x, y, z) * \mathrm{PSF}_z(x, y)\, \mathrm{d}z \tag{1}$$

where C is a constant, μ_a is the absorption coefficient of the fluorophore, F is the excitation fluence distribution, $*$ is the convolution, and PSF_Z is the point spread function at depth z.[22] Furthermore, the temporal decay of the fluorescence intensity is dependent on the excitation fluence-dependent photobleaching rate, which can be described as a first-order exponential decay (Figure 2a). μ_a can be simply modeled as a pure single-exponential function

$$I(x, y, t) = C \int \mu_{a0}(x, y, z) \mathrm{e}^{-F(x,y,z)Bt} F(x, y, z) * \mathrm{PSF}_z(x, y)\, \mathrm{d}z \tag{2}$$

where t is time, μ_{a0} is the initial absorption coefficient of the fluorophore, and B is a constant.

For conventional wide-field PIM, the lateral illumination profile is nearly Gaussian distributed. The nonuniform lateral excitation fluence complicates the analysis of the temporal decay of the fluorescence intensity at different lateral positions.

https://doi.org/10.1021/cbmi.3c00079
Chem. Biomed. Imaging 2023, 1, 843−851

In the previous work, the excitation fluence is assumed to be uniform along the lateral axes.[22] While such an approximation greatly simplifies the analysis, the nonuniform lateral excitation profile considerably limits the effective FOV of conventional wide-field PIM to the central illumination region, which scarifies not only the imaging throughput but also the sampling density.

As mentioned above, the excitation fluence in our system is uniform along the lateral axes and has a Gaussian distribution along the axial axes (Figure 2b). Hence, the excitation fluence F is only dependent on z. Thus, eq 2 turns into

$$I(x, y, t) = C \int \mu_{a0} e^{-F(Z)Bt} F(z) * \mathrm{PSF}_z(x, y)\, dz \quad (3)$$

and

$$F(z) = e^{-(z-z_0)^2/2\sigma_z^2} \quad (4)$$

where z_0 denotes the focal plane of the objective.

Similar with the previous report,[22] Taylor expansion and polynomial fitting of the fluorescence decay in eq 3 yields the PIM component I_n

$$I_n = C\frac{(-B)^n}{n!} \int \mu_{a0} F(z)^{n+1} * \mathrm{PSF}_z(x, y)\, dz \quad (5)$$

which is dependent on the $n + 1$ order fluence distribution.

Given that the excitation fluence in our system is a Gaussian distribution along the axial axes, the high-order F^{n+1} approached a delta function $\delta(z - z_0)$ and I_n became

$$I_n(x, y, n \gg 1) = C\frac{(-B)^n}{n!} \mu_{a0} \delta(z - z_0) * \mathrm{PSF}_{z_0}(x, y) \quad (6)$$

Compared with the conventional wide-field PIM, in which light is focused on the back focal plane of the objective, ffPIM focuses the light on the focal plane of the objective. Thereby, the center region of ffPIM is a thin layer with maximum intensity in the z-direction at the focal plane of the objective, while the center region of conventional wide-field microscopy is a small core near the objective (Figure 2b). The sharp intensity gradient along the z-direction renders ffPIM better optical sectioning capability than the conventional wide-field PIM. In addition, the excitation fluence of ffPIM in the $x-y$ plane is uniform, while the lateral excitation fluence of conventional wide-field microscopy at the sample plane has a Gaussian distribution. As a result, the uniform lateral illumination renders ffPIM with a larger FOV and higher sampling density than the conventional wide-field PIM with Gaussian illumination (Figure 2c).

To demonstrate the advantage of ffPIM, a simulation was performed by creating a 3D sample consisting of 100 randomly distributed fluorescent beads in a 100 × 100 × 100 volume. Simulation results I_0 to I_{10} of the beads show that higher order ffPIM was able to extract the signal of beads in a thinner section with increased SBR (Figure 2d).

Experimental Results of ffPIM

To characterize the performance of ffPIM, we first prepared a solid agar sample containing 40 nm diameter red fluorescent beads. For each layer, 100 images were acquired (30 ms exposure time, EM gain was set at 100, step size was 0.1 μm). The statistical axial full width at half maximum (FWHM) of the conventional image stack and 16th PIM component are shown in Figure 3a, which verify the effectiveness of ffPIM in improving optical sectioning. We also imaged cells with DNA replication origins labeled by 5-ethynyl-2'-deoxyuridine (EdU) pulse labeling. Similarly, we acquired 100 time-lapse images in each FOV. The statistical SBR of conventional images and 16th PIM component are shown in Figure 3b. The improvement of ffPIM was found to be nearly 2-fold, as shown in Figure 3c.

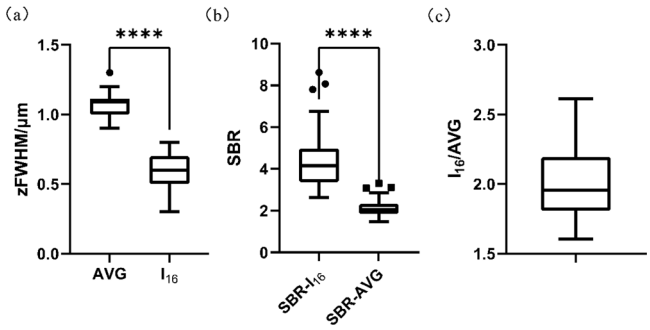

Figure 3. Performance characterization of ffPIM. The conventional image is the average image of the 100 time-lapse image. (a) Statistics of the axial FWHM of 21 beads in the conventional image stack and the 16th PIM component. (b) Statistics of the SBR of the 71 EdU signal in the conventional image and the 16th PIM component. (c) Improvement of SBR between the 16th PIM component and conventional image.

We next prepared a biological sample in which Lamin A/C is fluorescently labeled. The Lamin A/C sample is ideal for testing the optical sectioning capability of a microscopy system for two reasons. First, Lamin A/C is a main component of the nuclear lamina, with a small amount distributed within the nucleus. Second, the nucleus is located deep in a cell, usually a few micrometers away from the plasma surface, which is far beyond the working distance of TIRFM (~200 nm). Therefore, it is difficult to achieve a high signal-to-background ratio imaging using wide-field fluorescence microscopy. We acquired 100 time-lapse images using Gaussian illumination (Figure 4a) and flat-field illumination (Figure 4c), respectively. The wide-field image is the sum of the signal excited from the DOF of the objective. As the light intensity gradient of Gaussian illumination in the z-direction at the focal plane is less sharp than that of flat-field illumination, we expect a better optical sectioning capability with ffPIM. Indeed, the peri-nuclear distribution of lamin A/C was clearly observed by the averaged image of flat-field illumination shown in the left panel of Figure 4c. In contrast, the averaged image of Gaussian illumination in the left panel of Figure 4a failed to present the actual distribution of lamin A/C. Additionally, the intensity distribution in flat-field illumination images was much more uniform than that in Gaussian illumination images. These results confirm that flat-field illumination has better optical sectioning in the focal plane and a larger FOV than wide-field microscopy with Gaussian illumination. We next performed PIM analysis of both time lapse series, and I_{16} images are shown in the right panels of Figure 4a,c. It shows that, compared with the AVG images, PIM images have much lower background intensity within the nuclei (Figure 4b,d), indicating that PIM can effectively improve SBR. Notably, due to the nonuniform lateral excitation fluence, the PIM image (Figure 4a, right) of Gaussian illumination shows a smaller FOV than the AVG image (Figure 4a, left). For comparison, in flat-field illumination, the FOV remains constant. Hence, ffPIM has better optical sectioning in the

https://doi.org/10.1021/cbmi.3c00079
Chem. Biomed. Imaging 2023, 1, 843−851

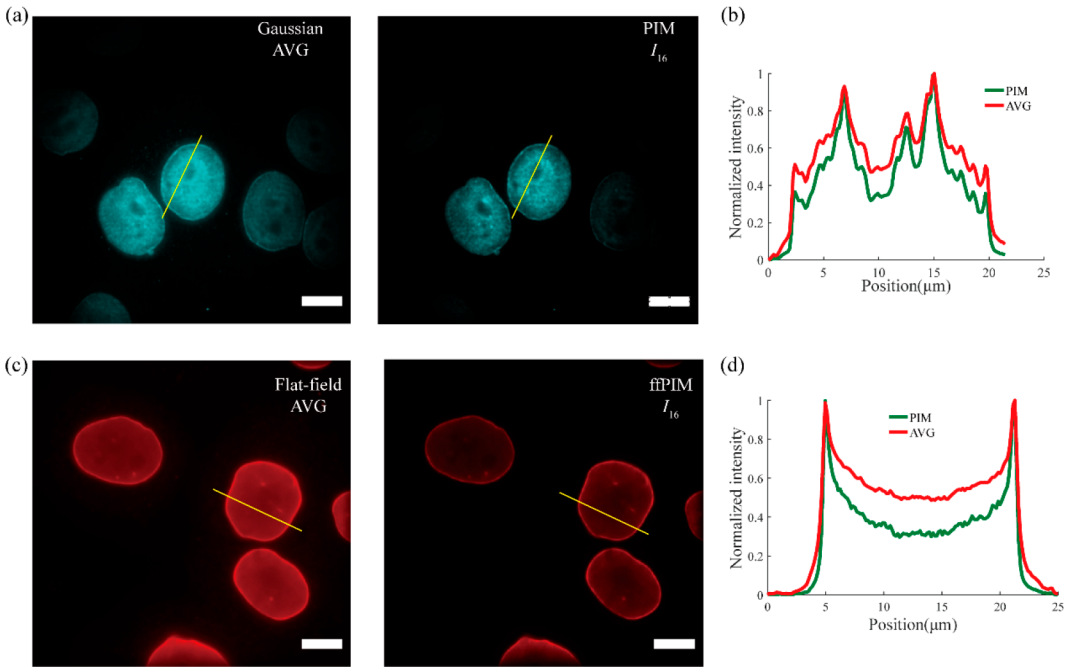

Figure 4. ffPIM has better optical sectioning at the focal plane and a larger FOV than wide-field microscopy with Gaussian illumination. (a) Images acquired by Gaussian illumination. Left: We collect 100 time-lapse images with 30 ms exposure time and then average. Right: PIM image I_{16}. (b) Intensity profile from yellow lines on (a). (c) Images acquired by flat-field illumination. Left: We collect 100 time-lapse images with 30 ms exposure time and then average. Right: PIM image I_{16}. (d) Intensity profile from yellow lines on (c). Green solid line: ffPIM; red solid line: AVG. The AVG images demonstrate the various illumination fluence between the two illumination modes along axial axes. The PIM images show ffPIM has better optical sectioning at the focal plane and a larger FOV than wide-field microscopy with Gaussian illumination. Scale bar, 10 μm.

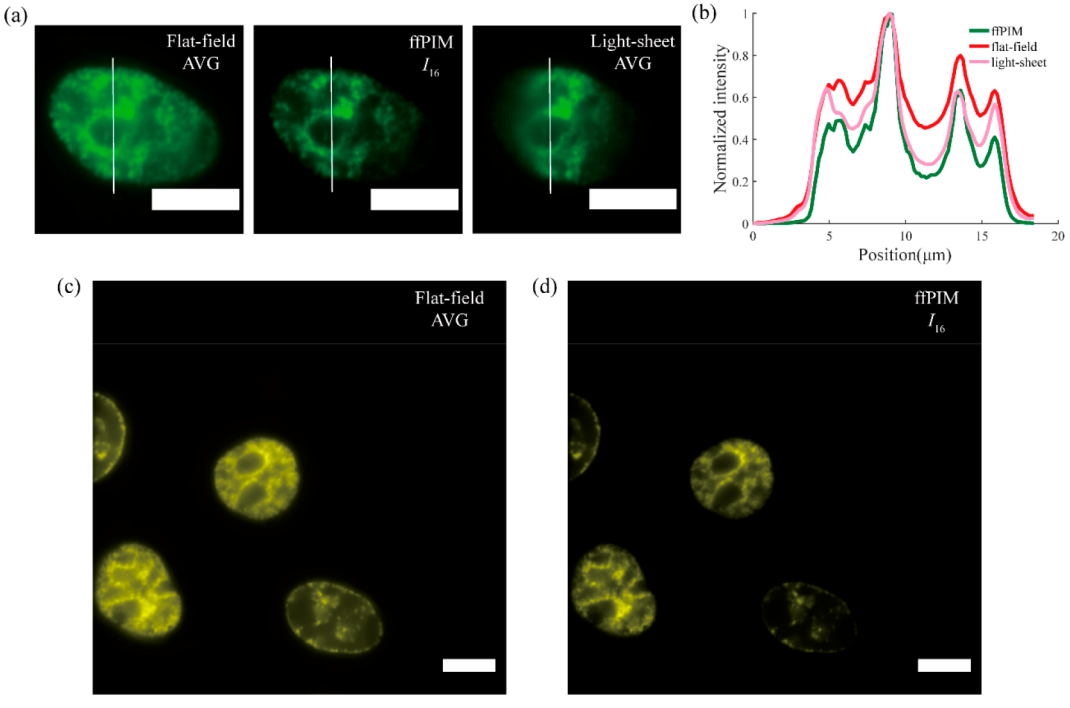

Figure 5. Comparison of ffPIM and light-sheet microscope. We prepared an EdU sample that labeled DNA replication origins within the nucleus. (a) Images of flat-field, ffPIM, and light-sheet in the same FOV. (b) Intensity profile from white lines on (a) shows the SBR of I_{16} was superior to that of the light-sheet image (green solid line: ffPIM; red solid line: flat-field; pink solid line: light-sheet). (c) Full-frame image of the nucleus. The camera in our system is an EMCCD camera with 512 × 512 pixels (DU-897D, Andor). (d) PIM image associated with I_{16}, which indicates ffPIM has high SBR and high throughput. Scale bar, 10 μm.

focal plane and a larger FOV than wide-field microscopy with Gaussian illumination.

To further characterize the optical sectioning capability of ffPIM, we performed a comparison with light-sheet microscopy for intranucleus imaging. Light-sheet microscopy with a high

https://doi.org/10.1021/cbmi.3c00079
Chem. Biomed. Imaging 2023, 1, 843−851

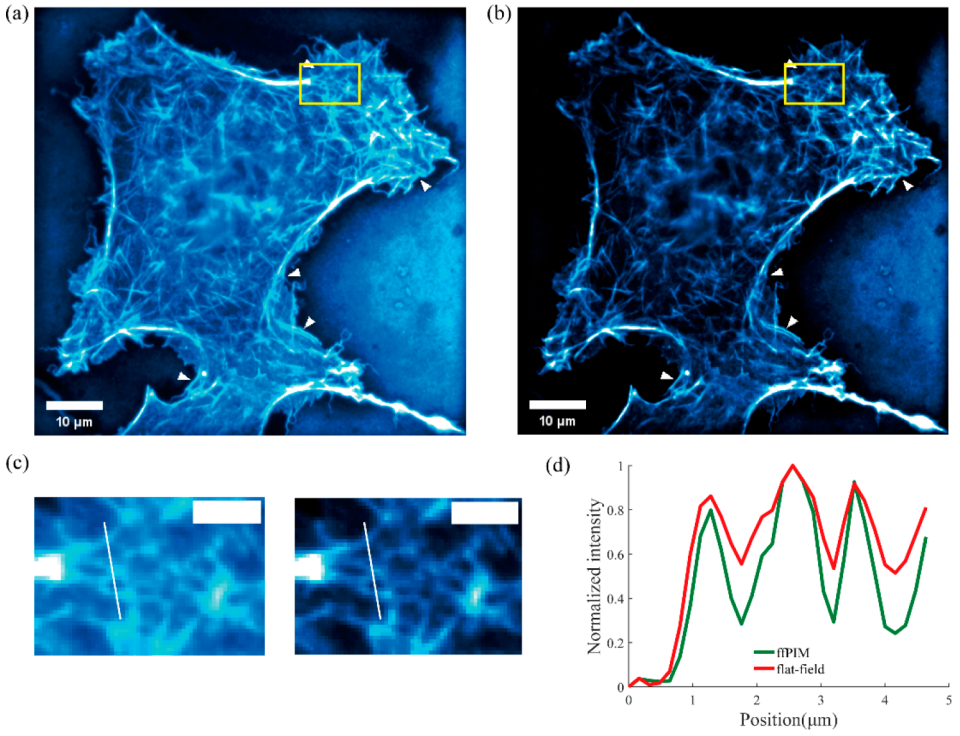

Figure 6. High-throughput and high SBR observation of actin. In the sample, actin was labeled with Actin stain 555. (a) Averaged image of 100 time-lapse images with 30 ms exposure time of actin by a flat-field microscope. (b) PIM image associated with I_{16}. The arrows in (a) and (b) indicate the part of the area where the SBR has improved. (c) Magnified sections from the boxed region in (a) and (b). (d) Intensity profile from white lines on (c) shows about a 2-fold improvement in SBR (red solid line: flat-field; green solid line: ffPIM). Scale bar, 10 μm.

numerical aperture (NA) objective is currently an effective wide-field imaging approach for high spatiotemporal imaging of nuclei.[7,36,37] We have developed a tilted light-sheet microscope and set the thickness of the light sheet to 1.6 μm and FOV to 5 μm for this comparison.[7] Hela S3 cells were pulse-labeled with EdU for 20 min to label the DNA replicating signal, followed by Alexa 647 labeling with the Click reaction (Methods). For comparison, we acquired 100 time-lapse flat-field images and light-sheet images in the same FOV (Figure 5a, left and right). Then, we calculated the PIM image, I_{16} (Figure 5a, middle). It is obvious that the SBR of I_{16} is better than that of the averaged light-sheet image (Figure 5b). In addition, it is well-known that there is a trade-off between the light-sheet thickness, i.e., SBR and FOV for light-sheet microscopy. In this regard, ffPIM shows a great advantage in the balance of SBR (Figure 5a,b) and FOV (Figure 5c,d), allowing high-throughput and high quality cellular imaging.

We used the first 10 images to calculate the 16th PIM image. Compared to the PIM image that used 100 images for the calculation, the structure computed with 10 images is sparser (Figure S1). Because we fitted the photobleaching parameters pixel by pixel, if the photobleaching rate is slow, PIM computation with 10 images would fail, and this pixel would be set to zero, leading to information loss. Hence, ffPIM is more suitable for applications where the photobleaching rate is fast. The faster the photobleaching rate, the fewer images needed for computation. Researchers can acquire images during photobleaching in several frames and then calculate an image with high SBR by ffPIM. Without ffPIM, these data will be considered unavailable. Hence, this method can save time to optimize labeling methods.

We next applied ffPIM to cellular structures with large size to emphasize the overall image quality with large FOV and high SBR. We labeled the actin cytoskeleton in BS-C-1 cells using actin stain 555 (cytoskeleton). As the spreading of BS-C-1 cells on the culture dish is generally tens of micrometers, its actin cytoskeleton is suitable for checking the quality of large FOV for single cell imaging. Flat-field imaging with the full camera sensor of a 82 × 82 μm^2 FOV shows a clear and even image of the whole actin network of a cell (Figure 6a). ffPIM further increases the SBR by extracting the signal in the focal plane and rejecting the out-of-focus background (Figure 6b). The arrows indicate an area where the SBR improves. The magnified area in the image (boxed area in Figure 6a,b) shows the blurred network structure due to the low SBR (Figure 6c, left). In contrast, we obtained a clear structure with PIM, which was about a 2-fold improvement of the SBR (Figure 6c, right and Figure 6d). This result confirms that ffPIM is a valuable method to observe biological samples with high-throughput and high SBR.

To test the performance of ffPIM in 3D volume imaging, we scanned the Lamin A/C sample along the depth axis, and a total of 100 time-lapse fluorescence images are captured at each depth for PIM calculation. The SBR of the flat-field fluorescence images is low due to crosstalk from the out of focal fluorescence signal (Figure 7a, top), while for the ffPIM images, owing to optical sectioning at the focal plane, the ring structure of nuclear lamina is more distinguishable, especially at the top and bottom depth of the nucleus (Figure 7b, bottom). Moreover, Figure 7a shows patterns of Lamin A/C at different planes of the nucleus detected by our system. The ring structure is most distinct near the central plane of the nucleus and blurred at the bottom and top of the nucleus. This

https://doi.org/10.1021/cbmi.3c00079
Chem. Biomed. Imaging 2023, 1, 843−851

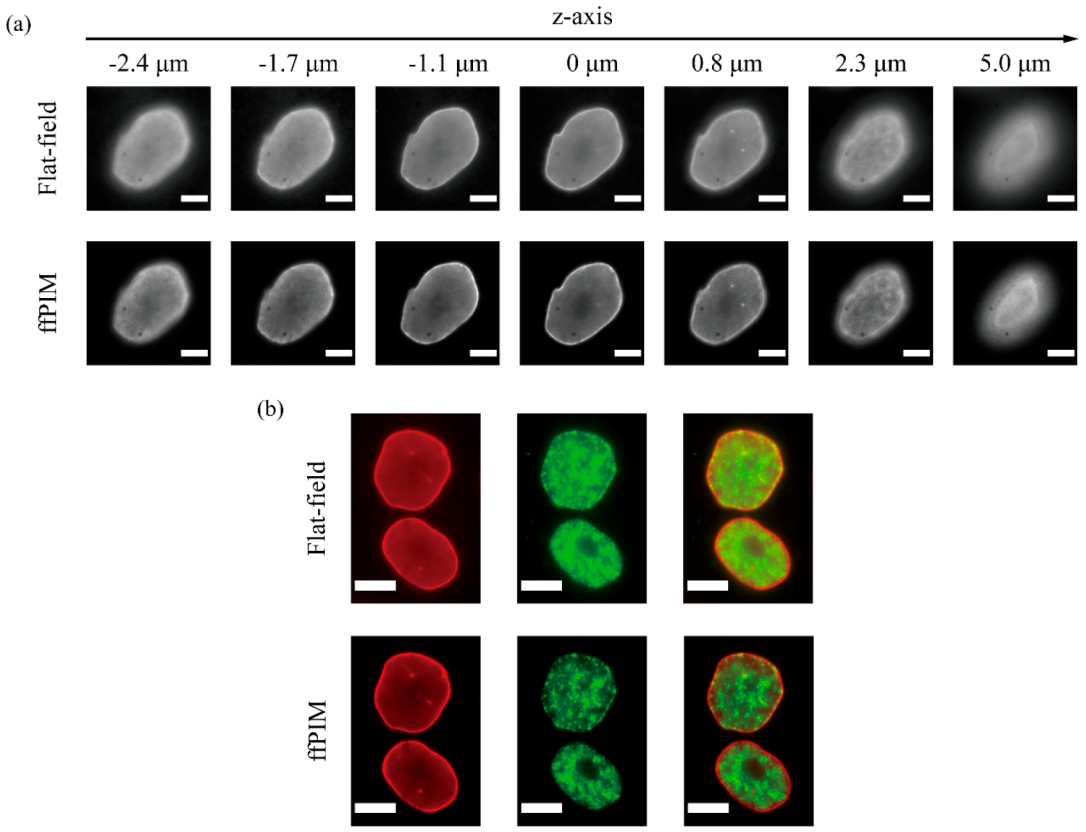

Figure 7. Optical sectioning image and dual-color image of ffPIM. (a) Images of Lamin A/C at different depths from the nucleus bottom to top. Upper images are averaged images captured by a flat-field microscope. Lower images are PIM images I_{16} of them, respectively. At each depth, we acquired 100 time-lapse images with 30 ms exposure time and then averaged. (b) Dual-color images of EdU and Lamin A/C. For both EdU and Lamin A/C images, 100 time-lapse images with 30 ms exposure time were acquired and then averaged. PIM images are associated with I_{16}. Scale bar, 10 μm.

proves that, in Gaussian illumination, the light intensity near the focal plane is not sharper than that of flat-field.

Finally, we applied ffPIM to dual-color imaging. Dual-color or multicolor imaging is usually used to investigate the colocalization relationship between different components. We captured images at the same FOV and depth of the sample dual-labeled with Lamin A/C and EdU. For each channel, we acquired 100 time-lapse images to calculate PIM images. It is clearly shown that ffPIM is able to improve the SBR in dual-color imaging (Figure 7b).

CONCLUSION

In summary, we present ffPIM which has fewer artifacts[22] and higher SBR and throughput than PIM with Gaussian illumination. Additionally, we demonstrate the volume imaging capability by acquiring samples at different depths. Finally, ffPIM can be easily implemented to a standard fluorescence microscope, which allows general laboratories to benefit from this technology.

Furthermore, due to the uniform distribution of light intensity in the *xy*-plane, molecules labeled by the same fluorescent dye or fluorescent protein have the same bleaching curve (eq 2). The curves can be regarded as fingerprints of different fluorophores. Supermultiplexed fluorescence imaging may be realized by applying this principle in the future.

METHODS

Flat-Field Microscopy Setup

The system is shown in Figure 1a. The optical system was built on a Nikon Eclipse Ti-E inverted microscope with 4 lasers of wavelengths 642 nm (2RU-VFL-P-1000-642-B1R, MPB Communications), 560 nm (2RU-VFL-P-1000-560-BIR, MPB Communications), 488 nm (2RU-VFL-P-300-488-BIR, MPB Communications), and 405 nm (OBIS, Coherent). Each laser beam is reflected by an aluminum mirror and a dichroic mirror and then pointed into an AOTF (AODS20160, Crystal Technology). Finally, laser beams are focused into a fiber adapter (SM1FCA, Thorlabs) and coupled into a customized multimode fiber, which is 20 m long with a 200 μm^2 square core, a 238 μm cladding diameter, and FC/APC connectors at both ends (WFANS 200 × 200/238 × 238, CeramOptec). The NA of the square-core fiber is 0.22. The optical fiber is blended into a circle with a radius of 15 cm and bound to a vibration motor with high frequency (~11 000 rpm) to remove speckles. The output beams pass through an objective lens (10×/NA 0.25, Olympus) to form a uniform square spot. Then, the square spot is reduced and focused on the sample plane by lens L2 (AC254-250-A-ML, Thorlabs) and an objective lens (Plan Apo 100× 1.49 oil immersion, Nikon). We can adjust the size of the field-of-view (FOV) by changing the focal length of L2. For example, a shorter focal length can create a larger FOV. Emitted fluorescence from the sample is collected by the same objective, filtered with a dichroic mirror (Di01-R405/488/561/635, Semrock) and an emission filter (FF01-446/523/600/677-25, Semrock), and imaged by a tube lens (f = 200 mm, MXA20696, Nikon) onto an EMCCD camera (DU-897D, Andor). The width of a square camera pixel corresponds to 157 nm in the sample. A detailed

https://doi.org/10.1021/cbmi.3c00079
Chem. Biomed. Imaging 2023, 1, 843−851

description of the customized light-sheet microscopy setup can be found in our published article.[7]

Sample Preparation

Cell Culture. All cell lines are cultured in DMEM (Invitrogen, C11995500BT) supplemented with 10% fetal bovine serum (FBS) (Hyclone, SV30087.02). To prevent bacterial contamination, 100 μg/mL penicillin and streptomycin (Invitrogen, 15140-122) are added to the culture medium. To avoid mycoplasma infection, 0.1 mg/mL mycoplasma inhibitors (C0288S, beyotime) are also added in the culture medium. All cell lines are routinely tested for potential mycoplasma contamination (C0296, beyotime), and all tests showed negative results. Cells are grown under standard cell culture conditions (5% CO_2, humidified atmosphere at 37 °C) and are plated on #1.5 glass bottom dishes (Standard Imaging Biotech., STGBD-036-1) over 24 h before sample preparation. For cell passage, cells were washed with pre-warmed PBS (Life Technologies, #14190500BT) 3 times and digested with 25% trypsin (Gibco, #25200-056).

EdU and Lamin A/C Sample

Hela S3 cells are seeded in a glass-bottom dish. When the cell density reaches about 70%, cultured cells are pulse-labeled with EdU (10 μM) for 20 min to label the replicating signal. Then, cells are fixed with 4% PFA (OKA, R20497), followed by PBS washing three times. Fixed samples are blocked with 5% BSA (sigma, B265988), followed by labeling with a click reaction by Alexa647 (Invitrogen, C10340). After that, samples are incubated with Lamin A/C primary antibody (Proteintech, 10298-1-AP), followed by incubation of secondary antibody (Gen Fluor, GFR-R). Finally, the samples are fixed again with 4% PFA.

Actin Sample

The kidney epithelial cell of an African green monkey, called the BS-C-1 cell line, was purchased from American Type Culture Collection (ATCC). BS-C-1 cells are grown on 35 mm, #1.5 glass bottom dishes (Standard Imaging Biotech., STGBD-036-1). On the day of sample preparation, cell density should be about 50−70%. Cells are fixed with 37 °C pre-warmed fixation buffer for 10 min, containing 4% EM-level paraformaldehyde and 0.1% glutaraldehyde in PBS. Then, the sample is washed three times with 2 mL of PBS. For quenching the background fluorescence of glutaraldehyde, we incubate the cells with 2 mL of 0.1% $NaBH_4$ solution in PBS for 7 min. The sample is washed three times with 2 mL PBS and then incubated for 30 min in PBS containing 5% BSA (Jackson, #001-000-162) and 0.5% Triton X-100 (Fisher Scientific) at room temperature. Actin stain 555 (Cytoskeleton, PHDH1-A) was diluted in the BSA and Triton solution as described above. Next, we incubate the sample for over 12 h with the appropriate dilution of Actin stain 555 in 4 °C. The sample is protected from light. After the incubation, the cells are washed 5 min with 2 mL PBS three times. After being washed with PBS, cells are fixed with post-fixation buffer for 10 min. The samples are washed 5 times with sterile water. Finally, the sterile water is removed, and the sample is ventilated, dried, sealed with parafilm, and stored at −20 °C.

■ ASSOCIATED CONTENT

Supporting Information

The Supporting Information is available free of charge at https://pubs.acs.org/doi/10.1021/cbmi.3c00079.

Image showing the different ffPIM effects with 100 and 10 images (PDF)

■ AUTHOR INFORMATION

Corresponding Author

Yujie Sun − *State Key Laboratory of Membrane Biology, Biomedical Pioneer Innovation Center (BIOPIC), School of Life Sciences, Peking University, Beijing 100871, China; National Biomedical Imaging Center, College of Future Technology, Peking University, Beijing 100871, China*; Email: sun_yujie@pku.edu.cn

Authors

Yizhi Qin − *State Key Laboratory of Membrane Biology, Biomedical Pioneer Innovation Center (BIOPIC), School of Life Sciences, Peking University, Beijing 100871, China*; orcid.org/0000-0002-0043-6416

Mengling Zhang − *State Key Laboratory of Membrane Biology, Biomedical Pioneer Innovation Center (BIOPIC), School of Life Sciences, Peking University, Beijing 100871, China*

Huiwen Hao − *State Key Laboratory of Membrane Biology, Biomedical Pioneer Innovation Center (BIOPIC), School of Life Sciences, Peking University, Beijing 100871, China*

Boxin Xue − *College of Chemistry and Molecular Engineering, Peking University, Beijing 100871, China*

Jiahao Niu − *State Key Laboratory of Membrane Biology, Biomedical Pioneer Innovation Center (BIOPIC), School of Life Sciences, Peking University, Beijing 100871, China*; orcid.org/0000-0003-4273-4398

Complete contact information is available at: https://pubs.acs.org/10.1021/cbmi.3c00079

Author Contributions

Y.Q. and Y.S. conceived the original idea and supervised the project. Y.Q. built the flat-field microscope, performed the experiments, analyzed the results, made the simulations, and drafted the manuscript. B.X. and Y.Q. built the ImTLSM system. M.Z., J.N., and H.H. performed sample preparation. All authors contributed to the Article and approved the submitted version.

Notes

The authors declare no competing financial interest.

■ ACKNOWLEDGMENTS

We thank Standard Imaging (Beijing) Biotechnology Co., Ltd. for help with the actin sample preparation. We thank Dr. Weisong Zhao for helpful advice. We thank Dr. Siying Qin at the National Center for Protein Sciences at Peking University in Beijing, China, for technical help on Imaris. This work is supported by grants from the National Key R&D Program of China Nos. 2021YFF0700304 and 2022YFA3401100 and the National Science Foundation of China 22127804.

■ REFERENCES

(1) Thul, P. J.; Åkesson, L.; Wiking, M.; Mahdessian, D.; Geladaki, A.; Ait Blal, H.; Alm, T.; Asplund, A.; Björk, L.; Breckels, L. M.; Bäckström, A.; Danielsson, F.; Fagerberg, L.; Fall, J.; Gatto, L.; Gnann, C.; Hober, S.; Hjelmare, M.; Johansson, F.; Lee, S.; Lindskog, C.; Mulder, J.; Mulvey, C. M.; Nilsson, P.; Oksvold, P.; Rockberg, J.; Schutten, R.; Schwenk, J. M.; Sivertsson, A.; Sjöstedt, E.; Skogs, M.; Stadler, C.; Sullivan, D. P.; Tegel, H.; Winsnes, C.; Zhang, C.; Zwahlen, M.; Mardinoglu, A.; Pontén, F.; von Feilitzen, K.; Lilley, K. S.; Uhlén, M.; Lundberg, E. A Subcellular Map of the Human Proteome. *Science* **2017**, *356* (6340), No. eaal3321.

(2) Stelzer, E. H. K.; Strobl, F.; Chang, B.-J.; Preusser, F.; Preibisch, S.; McDole, K.; Fiolka, R. Light Sheet Fluorescence Microscopy. *Nature Reviews Methods Primers* **2021**, *1* (1), 73.

(3) Jonkman, J.; Brown, C. M.; Wright, G. D.; Anderson, K. I.; North, A. J. Tutorial: Guidance for Quantitative Confocal Microscopy. *Nat. Protoc.* **2020**, *15* (5), 1585−1611.

(4) Scheele, C. L. G. J.; Herrmann, D.; Yamashita, E.; Lo Celso, C.; Jenne, C. N.; Oktay, M. H.; Entenberg, D.; Friedl, P.; Weigert, R.; Meijboom, F. L. B.; Ishii, M.; Timpson, P.; van Rheenen, J. Multiphoton Intravital Microscopy of Rodents. *Nature Reviews Methods Primers* **2022**, *2* (1), 89.
(5) Kim, J.; Wojcik, M.; Wang, Y.; Moon, S.; Zin, E. A.; Marnani, N.; Newman, Z. L.; Flannery, J. G.; Xu, K.; Zhang, X. Oblique-Plane Single-Molecule Localization Microscopy for Tissues and Small Intact Animals. *Nat. Methods* **2019**, *16* (9), 853−857.
(6) Yang, B.; Chen, X.; Wang, Y.; Feng, S.; Pessino, V.; Stuurman, N.; Cho, N. H.; Cheng, K. W.; Lord, S. J.; Xu, L.; Xie, D.; Mullins, R. D.; Leonetti, M. D.; Huang, B. Epi-Illumination SPIM for Volumetric Imaging with High Spatial-Temporal Resolution. *Nat. Methods* **2019**, *16* (6), 501−504.
(7) Xue, B.; Zhou, C.; Yizhi, Q.; Yongzheng, L.; Yuao, S.; Lei, C.; Shipeng, S.; Yongliang, L.; Mengling, Z.; Chaoying, S.; Renxi, H.; Qian, P. S.; Sun, Y. PN-Imtlsm Facilitates High-Throughput Low Background Single-Molecule Localization Microscopy Deep in the Cell. *Biophysics Reports* **2021**, *7* (4), 313.
(8) Dunsby, C. Optically Sectioned Imaging by Oblique Plane Microscopy. *Opt. Express* **2008**, *16* (25), 20306−20316.
(9) Galland, R.; Grenci, G.; Aravind, A.; Viasnoff, V.; Studer, V.; Sibarita, J. B. 3D High- and Super-Resolution Imaging Using Single-Objective SPIM. *Nat. Methods* **2015**, *12* (7), 641−4.
(10) Maioli, V.; Chennell, G.; Sparks, H.; Lana, T.; Kumar, S.; Carling, D.; Sardini, A.; Dunsby, C. Time-Lapse 3-D Measurements of a Glucose Biosensor in Multicellular Spheroids by Light Sheet Fluorescence Microscopy in Commercial 96-Well Plates. *Sci. Rep.* **2016**, *6*, 37777.
(11) Sikkel, M. B.; Kumar, S.; Maioli, V.; Rowlands, C.; Gordon, F.; Harding, S. E.; Lyon, A. R.; MacLeod, K. T.; Dunsby, C. High Speed sCMOS-Based Oblique Plane Microscopy Applied to the Study of Calcium Dynamics in Cardiac Myocytes. *Journal of Biophotonics* **2016**, *9* (3), 311−323.
(12) Patel, K. B.; Liang, W.; Casper, M. J.; Voleti, V.; Li, W.; Yagielski, A. J.; Zhao, H. T.; Perez Campos, C.; Lee, G. S.; Liu, J. M.; Philipone, E.; Yoon, A. J.; Olive, K. P.; Coley, S. M.; Hillman, E. M. C. High-Speed Light-Sheet Microscopy for the In-situ Acquisition of Volumetric Histological Images of Living Tissue. *Nature Biomedical Engineering* **2022**, *6*, 569.
(13) Yang, B.; Lange, M.; Millett-Sikking, A.; Zhao, X.; Bragantini, J.; VijayKumar, S.; Kamb, M.; Gómez-Sjöberg, R.; Solak, A. C.; Wang, W.; Kobayashi, H.; McCarroll, M. N.; Whitehead, L. W.; Fiolka, R. P.; Kornberg, T. B.; York, A. G.; Royer, L. A. Daxi—High-Resolution, Large Imaging Volume and Multi-View Single-Objective Light-Sheet Microscopy. *Nat. Methods* **2022**, *19*, 461.
(14) Bimber, O.; Schedl, D. Light-Field Microscopy: A Review. *Journal of Neurology & Neuromedicine* **2019**, *4*, 1−6.
(15) Huang, B.; Wang, W.; Bates, M.; Zhuang, X. Three-Dimensional Super-Resolution Imaging by Stochastic Optical Reconstruction Microscopy. *Science* **2008**, *319* (5864), 810.
(16) Baddeley, D.; Cannell, M. B.; Soeller, C. Three-Dimensional Sub-100 nm Super-Resolution Imaging of Biological Samples Using a Phase Ramp in the Objective Pupil. *Nano Research* **2011**, *4* (6), 589−598.
(17) Shechtman, Y.; Sahl, S. J.; Backer, A. S.; Moerner, W. E. Optimal Point Spread Function Design for 3D Imaging. *Phys. Rev. Lett.* **2014**, *113* (13), 133902.
(18) Lee, J. S.; Wee, T. L.; Brown, C. M. Calibration of Wide-Field Deconvolution Microscopy for Quantitative Fluorescence Imaging. *Journal of biomolecular techniques: JBT* **2014**, *25* (1), 31−40.
(19) Murray, J. M. Methods for Imaging Thick Specimens: Confocal Microscopy, Deconvolution, and Structured Illumination. *Cold Spring Harbor Protocols* **2011**, *2011* (12), pdb.top066936.
(20) Murray, J. M.; Appleton, P. L.; Swedlow, J. R.; Waters, J. C. Evaluating Performance in Three-Dimensional Fluorescence Microscopy. *J. Microsc.* **2007**, *228* (3), 390−405.
(21) Wallace, W.; Schaefer, L. H.; Swedlow, J. R. A Workingperson's Guide to Deconvolution in Light Microscopy. *BioTechniques* **2001**, *31* (5), 1076−1097.
(22) Li, C. Y.; Gao, L.; Liu, Y.; Wang, L. H. V. Optical Sectioning by Wide-Field Photobleaching Imprinting Microscopy. *Appl. Phys. Lett.* **2013**, *103* (18), 183703.
(23) Gao, L.; Garcia-Uribe, A.; Liu, Y.; Li, C.; Wang, L. V. Photobleaching Imprinting Microscopy: Seeing Clearer And Deeper. *Journal of Cell Science* **2014**, *127* (2), 288.
(24) Gao, L.; Zhu, L.; Li, C.; Wang, L. V. Nonlinear Light-Sheet Fluorescence Microscopy by Photobleaching Imprinting. *Journal of The Royal Society Interface* **2014**, *11* (93), 20130851.
(25) Yao, J.; Wang, L.; Li, C.; Zhang, C.; Wang, L. V. Photoimprint Photoacoustic Microscopy for Three-Dimensional Label-Free Sub-diffraction Imaging. *Phys. Rev. Lett.* **2014**, *112* (1), 014302.
(26) Xiong, B.; Han, X.; Wu, J.; Xie, H.; Dai, Q. Improving Axial Resolution of Bessel Beam Light-Sheet Fluorescence Microscopy by Photobleaching Imprinting. *Opt. Express* **2020**, *28* (7), 9464−9476.
(27) Zhuang, C. W.; Li, X. Y.; Zhang, Y. L.; Kong, L. J.; Xie, H.; Dai, Q. H. Photobleaching Imprinting Enhanced Background Rejection in Line-Scanning Temporal Focusing Microscopy. *Front Chem.* **2020**, *8*, 1.
(28) Khaw, I.; Croop, B.; Tang, J.; Möhl, A.; Fuchs, U.; Han, K. Y. Flat-Field Illumination for Quantitative Fluorescence Imaging. *Opt. Express* **2018**, *26* (12), 15276−15288.
(29) Möhl, A.; Fuchs, U. Exploring the Unlimited Possibilities of Modular Aspheric Gauss to Top-Hat Beam Shaping. *Adv. Opt. Techn* **2016**, *5* (3), 201−210.
(30) Rowlands, C. J.; Ströhl, F.; Ramirez, P. P. V.; Scherer, K. M.; Kaminski, C. F. Flat-Field Super-Resolution Localization Microscopy with a Low-Cost Refractive Beam-Shaping Element. *Sci. Rep.* **2018**, *8* (1), 5630.
(31) Stehr, F.; Stein, J.; Schueder, F.; Schwille, P.; Jungmann, R. Flat-top TIRF Illumination Boosts DNA-PAINT Imaging and Quantification. *Nat. Commun.* **2019**, *10* (1), 1268.
(32) Voelkel, R.; Weible, K. J. Laser beam homogenizing: limitations and constraints. In *Proc. SPIE 7102, Optical Fabrication, Testing, and Metrology III*; SPIE, 2008; Vol. *7102*, p 71020J.
(33) Douglass, K. M.; Sieben, C.; Archetti, A.; Lambert, A.; Manley, S. Super-Resolution Imaging of Multiple Cells by Optimized Flat-Field Epi-Illumination. *Nat. Photonics* **2016**, *10*, 705.
(34) Deschamps, J.; Rowald, A.; Ries, J. Efficient Homogeneous Illumination and Optical Sectioning for Quantitative Single-Molecule Localization Microscopy. *Opt. Express* **2016**, *24* (24), 28080−28090.
(35) Zhao, Z.; Xin, B.; Li, L.; Huang, Z.-L. High-Power Homogeneous Illumination for Super-Resolution Localization Microscopy with Large Field-of-View. *Opt. Express* **2017**, *25* (12), 13382−13395.
(36) Gebhardt, J. C.; Suter, D. M.; Roy, R.; Zhao, Z. W.; Chapman, A. R.; Basu, S.; Maniatis, T.; Xie, X. S. Single-Molecule Imaging of Transcription Factor Binding to DNA in Live Mammalian Cells. *Nat. Methods* **2013**, *10* (5), 421−6.
(37) Chen, B. C.; Legant, W. R.; Wang, K.; Shao, L.; Milkie, D. E.; Davidson, M. W.; Janetopoulos, C.; Wu, X. S.; Hammer, J. A., 3rd; Liu, Z.; English, B. P.; Mimori-Kiyosue, Y.; Romero, D. P.; Ritter, A. T.; Lippincott-Schwartz, J.; Fritz-Laylin, L.; Mullins, R. D.; Mitchell, D. M.; Bembenek, J. N.; Reymann, A. C.; Bohme, R.; Grill, S. W.; Wang, J. T.; Seydoux, G.; Tulu, U. S.; Kiehart, D. P.; Betzig, E. Lattice Light-Sheet Microscopy: Imaging Molecules to Embryos at High Spatiotemporal Resolution. *Science* **2014**, *346* (6208), 1257998.

https://doi.org/10.1021/cbmi.3c00079
Chem. Biomed. Imaging 2023, 1, 843−851